PAPER

Check for updates

Rational methodology of V–Al alloy-electrorefining protocols promotes high purity vanadium metal

Qiwen Zhang, [abcd] Yong Fan, *[abcd] Yimin Zhang, [abcd] Peng Liu, [abcd] Hong Liu, [abcd] Zihanyu Zhang [abcd] and Xiuqiong Fu [abcd]

Molten salt electrolysis is a promising method for producing metallic vanadium, overcoming the limitations of conventional processes, such as high purity requirements for raw materials and high impurity content. This study introduces an innovative approach utilizing soluble vanadium–aluminum alloy anodes in KCl–LiCl molten salt, where vanadium is dissolved as V^{2+} and V^{3+}. Optimal conditions were identified as 0.3 A cm^{-2} current density, 500 °C temperature, and 6 h duration. High purity metallic vanadium was prepared under these conditions, and the electrolysis efficiency reached 89.53%. Electrochemical analysis revealed three reduction processes: Al(III) → Al, V(III) → V(II) and V(II) → V. In molten salts, vanadium ions existed in coordination forms as VCl_2, VCl_3, VCl_4^{2-}, and VCl_6^{3-}, while aluminum ions were present as $AlCl_4^-$. The process was confirmed as diffusion-controlled, with calculated V(III) diffusion coefficients. Nucleation mechanism analysis demonstrated dual vanadium deposition pathways: instantaneous and progressive nucleation. Fluoride ions were found to enhance reaction kinetics through chloride substitution in aluminum complexes, increasing free chloride availability for vanadium coordination and improving ion mobility. The developed method offers significant advantages in energy efficiency and product quality compared to traditional metallurgical approaches, providing insights for optimization of molten salt electrolysis systems in refractory metal production.

1. Introduction

Metallic vanadium is a silver-gray metal which, due to its unique physical and chemical properties, performs well under various environmental conditions.[1–3] In addition to being an important stabilizer and strengthening agent in the steel and aerospace industries, vanadium and its alloy have good prospects in nuclear fusion, hydrogen storage, superconducting materials.[4–6] These advantages arise from their properties such as low activation characteristics under neutron irradiation, high thermal conductivity, high-temperature strength, good creep resistance, and processing performance, which are crucial for high-temperature environments.[7–9] Moreover, vanadium and its alloy can be used as negative electrode materials for multi-phase oxygen electrode alloys, making it possible to manufacture higher-efficiency batteries, with electric vehicles being a potential market for

these batteries.[10,11] The main method for producing metallic vanadium is the thermal reduction process by using vanadium pentoxide (V_2O_5) or vanadium trioxide (V_2O_3) as raw materials and employing reducing agents such as Ca, Mg, Al, or C. Recent research has seen extensive efforts to optimize these thermal reduction processes, aiming to enhance the kinetics of aluminothermic reactions and vanadium recovery rates. The primary process involves the aluminothermic reduction of high-purity V_2O_5 to produce AlV85 (approximately 85 wt% vanadium and 15 wt% aluminum), followed by two rounds of vacuum electron beam melting to obtain vanadium metal with 99.0–99.5% purity. However, these processes result in challenges such as extended production cycles, stringent requirements for raw vanadium materials, and elevated impurity levels. Consequently, there is a need to develop a method for producing high-purity metallic vanadium.[12–15]

Among existing vanadium production systems, molten salt electrolysis technology is the most promising method.[16–18] It has the advantages of low reaction temperature, high efficiency, and high product purity and is widely used for metal purification. In the traditional vanadium refining process, AlV85 alloy requires vacuum electron beam melting, which necessitates temperatures above 1500 °C. In contrast, the molten salt electrolysis process typically operates below 1000 °C, significantly reducing energy consumption. The molten salt electrolysis process is influenced by factors such as electrode properties, salt

School of Resource and Environmental Engineering, Wuhan University of Science and Technology, Wuhan 430081, Hubei Province, China. E-mail: fanyong@wust.edu.cn

State Environmental Protection Key Laboratory of Mineral Metallurgical Resources Utilization and Pollution Control, Wuhan University of Science and Technology, Wuhan 430081, Hubei Province, China

Collaborative Innovation Center of Strategic Vanadium Resources Utilization, Wuhan University of Science and Technology, Wuhan 430081, Hubei Province, China

Hubei Provincial Engineering Technology Research Center of High Efficient Cleaning Utilization for Shale Vanadium Resource, Wuhan University of Science and Technology, Wuhan 430081, Hubei Province, China

composition, and temperature. The choice of electrode material for electrolysis plays a significant role in the process.[19–21] Methods like Fray–Farthing–Chen (FFC),[22,23] OS,[24] and Solid Oxygen Ionic Membrane (SOM) have been considered promising for producing vanadium.[25] Recent research has focused on optimizing these methods, for example, by developing novel cathode structures for FFC, investigating different anode compositions and feeding mechanisms for OS, and exploring stable oxygen-ion-conducting membranes for SOM. However, the graphite anode is easily consumed during electrolysis. And vanadium oxides are almost insoluble in the molten chlorides. The solid electro-deoxidation process is very slow and vanadium oxides must be obtained by a complex process.

Vanadium–aluminum (V–Al) alloy, as a type of vanadium alloy, can be advantageous compared to traditional reduction processes, which use vanadium oxides. During the preparation of V–Al alloy, by-products of aluminum can be easily washed away by acid or alkali. And the reduction process using aluminum lowers the reaction energy consumption, thus improving the yield of the metallic vanadium. However, the use of V–Al alloy also has certain limitations.[26] During the electrolysis process, impurities such as Al may deposit on the cathode, which may lead to a decrease in the purity of the obtained metallic vanadium. To address this issue, a viable strategy involves the introduction of potassium fluoride (KF) into the molten salt system. Under certain conditions, KF demonstrates the capability to form stable coordination complexes with aluminum ions (Al^{3+}), thereby modifying the coordination architecture of the molten salt medium.[27] This structural reorganization effectively inhibits the electrochemical deposition of metallic aluminum through two primary mechanisms.

The molten salt electrolyte, as a carrier for the electrolysis process, also significantly affects the reaction. Alkali metal and alkaline earth metal chlorides are the most stable and inexpensive molten salts and are ideal for the molten salt system. Due to the relatively low decomposition voltage of $CaCl_2$,[28] the electrochemical behavior in $CaCl_2$-based[29] electrolytes is accompanied by calcium deposition, which interferes with the electrolysis process. Compared to the NaCl–KCl[30,31] electrolyte, the KCl–LiCl[32] system offers a lower eutectic temperature. Owing to the small ionic radius and high migration rate of Li ions, it exhibits good ionic conductivity, thereby reducing energy consumption costs to some extent. Additionally, the KCl–LiCl[33] system possesses a wide electrochemical window. The standard electrode potentials of K and Li are lower than that of vanadium, meaning their deposition does not interfere with the reaction. To summarize, this study employs the KCl–LiCl system as the molten salt for the electrolysis process.

Therefore, this study proposes a simple, low-energy method for the production of metallic vanadium through electrolysis of soluble V–Al alloy anodes in a KCl–LiCl molten salt system. The schematic diagram is shown in Fig. 1. The study optimizes electrolysis conditions such as anode current density, reaction temperature, and time, and investigates the reduction and diffusion processes in the KCl–LiCl molten salt through various electrochemical tests. The diffusion coefficients and nucleation patterns of vanadium ions are calculated. The addition of fluoride (F) ions changes the electrochemical properties and
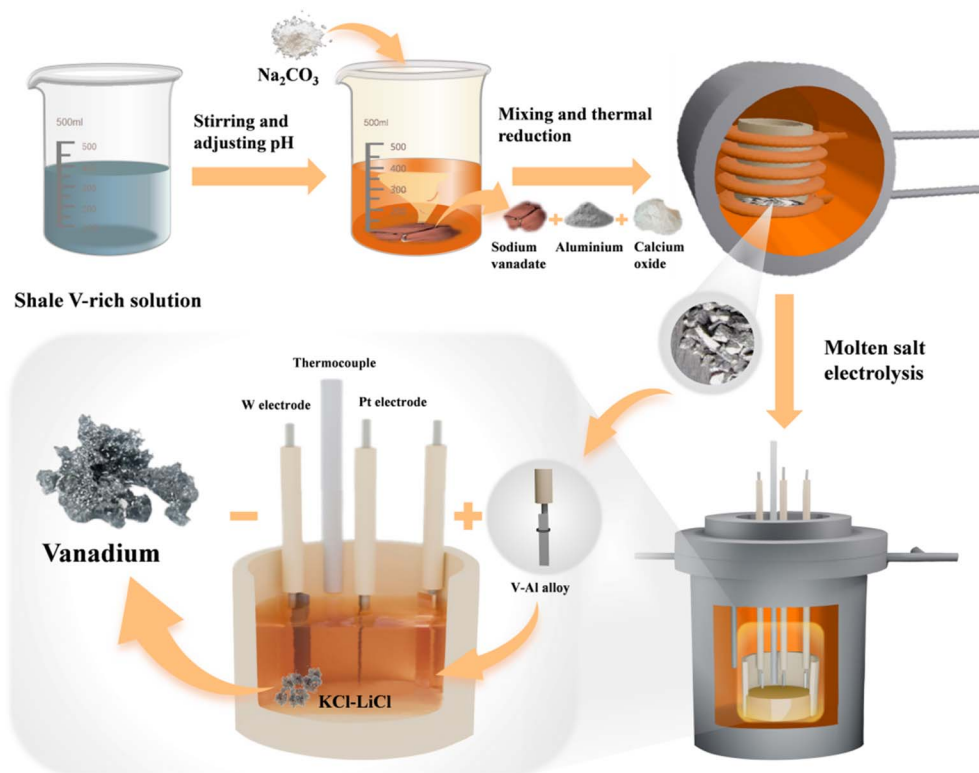

Fig. 1 Schematic diagram for the preparation of metallic vanadium by the electrolysis.

reduction process, and their effects on the product are analyzed. Additionally, molecular dynamics (MD) and density functional theory (DFT) are combined to study the bonding processes in the reaction system through radial distribution functions and analyze the atomic interactions between ions during the electrolysis process.

2. Experimental

2.1 Preparation of metallic vanadium

In this study, a eutectic salt of KCl and LiCl in a molar ratio of 55 : 45 (KCl, purity 99.8%, LiCl, purity 99.8%, purchased from Macklin Biochemical Co., Ltd) was used as the electrolyte, with a total weight of 100 g. Before electrolysis, KCl and LiCl were mixed uniformly and vacuum-dried at 300 °C for 3 h to remove excess moisture, then heated to 500 °C and maintained at this temperature for 12 h for pre-electrolysis. After pre-electrolysis, electrochemical tests and deposition were performed. Vanadium ions were introduced into the electrolyte in the form of V–Al alloy (65% vanadium content, which is prepared by hydrolyzing vanadium-rich shale solution to obtain sodium vanadate, then mixing it with aluminum powder and CaO for thermal reduction, as shown in Fig. 2. Other impurities meet the standards in Table 1). Aluminum powder (99.9% purity, purchased from Shanghai Aladdin Biochemical Technology Co.) and calcium oxide (98% purity, purchased from Shanghai Aladdin Biochemical Technology Co.) were used. The experimental setup is shown in Fig. 3, and the entire experiment was carried out under an argon atmosphere. The electrolytic cell consisted of an alumina crucible (inner diameter: 80 mm, height: 100 mm) containing KCl–LiCl eutectic salt. The inter-electrode distance was fixed at 50 mm. V–Al alloy and tungsten plates (1 mm thick, 2 mm wide, 99.99% purity) were used as the anode and cathode, respectively, in a two-electrode system for the preparation of metallic vanadium. Later, a three-electrode system was used for electrochemical experiments. A platinum wire (1 mm, 99.99% purity) was used as the reference electrode, with a graphite rod (5 mm, 99.99% purity) as the counter electrode, and the working electrode was the V–Al alloy. To make

Table 1 Composition analysis of vanadium aluminum alloy

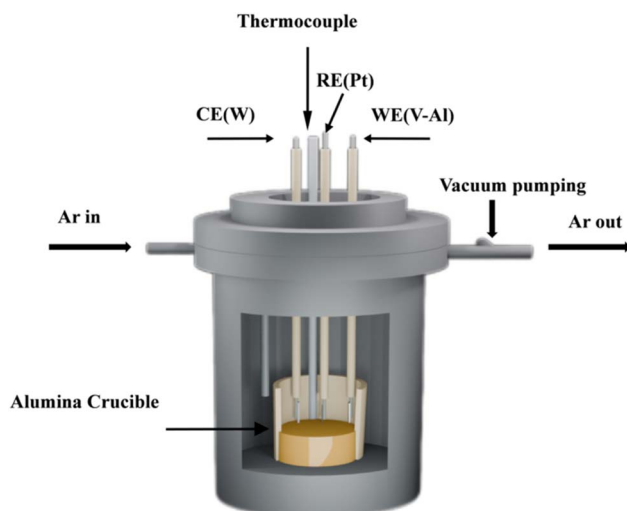| Element	V	Al	Fe	C	N	O
Composition (wt%)	66.65	33.14	0.08	0.07	0.02	0.12

Fig. 3 Schematic of the experimental apparatus used for molten salt electrolysis.

the experiment more comparable, the reference potential was converted to Cl_2/Cl^-. For calibration of the reference potential, a platinum–carbon rod (3 mm, 99.99% purity) was used as the working electrode, and a platinum rod was used as the reference electrode. Prior to the experiment, the electrodes were polished with sandpaper, then cleaned with alcohol and dried.

2.2 Products characterization

After electrolysis, the cathode product was cleaned with deionized water under ultrasonic treatment, followed by soaking in dilute HCl solution, and then dried at 80 °C for 6 h. The electrochemical tests were recorded with the Nova 2.1 software
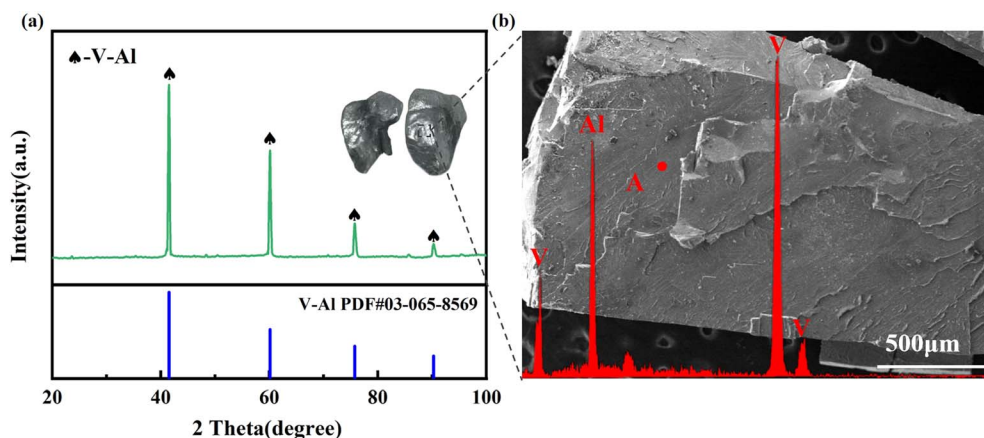
Fig. 2 (a) XRD of V–Al alloy prepared from sodium vanadate; (b) SEM of V–Al alloy prepared from sodium vanadate and the results of EDS analysis at point A.

package controlled by AutoLab (PGSTAT 302 N). Transient electrochemical techniques were employed to study the electrochemical behavior in the KCl–LiCl system. A glass funnel (outer diameter 35 mm, inner diameter 30 mm, tube diameter 8 mm, total length 50 cm) was quickly inserted into the molten salt before and after electrolysis at 500 °C to draw up the molten salt and then removed. The collected salt was vacuum-dried. The V content in the cooled molten salt and the valence state of vanadium ions before and after electrolysis were tested using an inductively coupled plasma optical emission spectrometer (ICP-OES, PerkinElmer 8300, PerkinElmer, Waltham, Mass, USA) and an X-ray photoelectron spectrometer (XPS, Thermo Scientific K-Alpha). The microscopic structure and morphology of the cathode deposits were studied using a scanning electron microscope (SEM, JSM-IT300, JEOL, Tokyo, Japan), energy dispersive spectrometer (EDS, Oxford Instruments, Oxford, UK), and X-ray diffraction (XRD, Rigaku, Tokyo, Japan). Using a DXR Raman microscope and compared with simulated values. The simulation calculations involved in this article were all performed using Materials Studio (MS, 2018version), quantum chemistry calculations were completed using DMol3 and Castep modules, and MD calculations were mainly based on the 110 Forcite module, using VESTA software as a visualization tool.

3. Results and discussion

3.1 Optimal conditions for electrolyzing metallic vanadium

During the electrolysis process, the electrolytic conditions significantly influence the preparation of metallic vanadium.

This study investigates the effects of anode current density, electrolysis temperature, and electrolysis duration on the electrolysis process. Under conditions where the number of transferred electrons is unknown, the electrolytic efficiency of vanadium ions was analyzed as a key reference metric, with results illustrated in Fig. 4. As a critical parameter in the process, electrolytic efficiency is defined as the ratio of the actual mass of deposited product to the dissolved mass at the anode. Higher electrolytic efficiency indicates reduced vanadium ion loss, improved utilization of vanadium ions, correspondingly higher current efficiency, and lower energy consumption. The electrolytic efficiency is calculated using eqn (1) and (2) as evaluation criteria:

$$\omega = \frac{m}{m_c} \times 100\% \tag{1}$$

$$m_c = (m_0 - m') \times \alpha_V \tag{2}$$

where m is actual deposition quality (g), m_c is anodic stripping quality (g), m_0 is quality of vanadium aluminum alloy before electrolysis (g), m' is quality of vanadium aluminum alloy after electrolysis (g) and α_V is the mass fraction of V in vanadium aluminum alloy.

Under the conditions of an anode current density of 0.3 A cm^{-2} and a cathode current density of 0.2 A cm^{-2}, electrolysis of the V–Al alloy was performed, and the cell voltage and electrolysis time were recorded, as shown in Fig. 4a. It can be observed that the electrolysis process can be divided into three stages. In the initial stage, the voltage rises continuously, which may be due to the
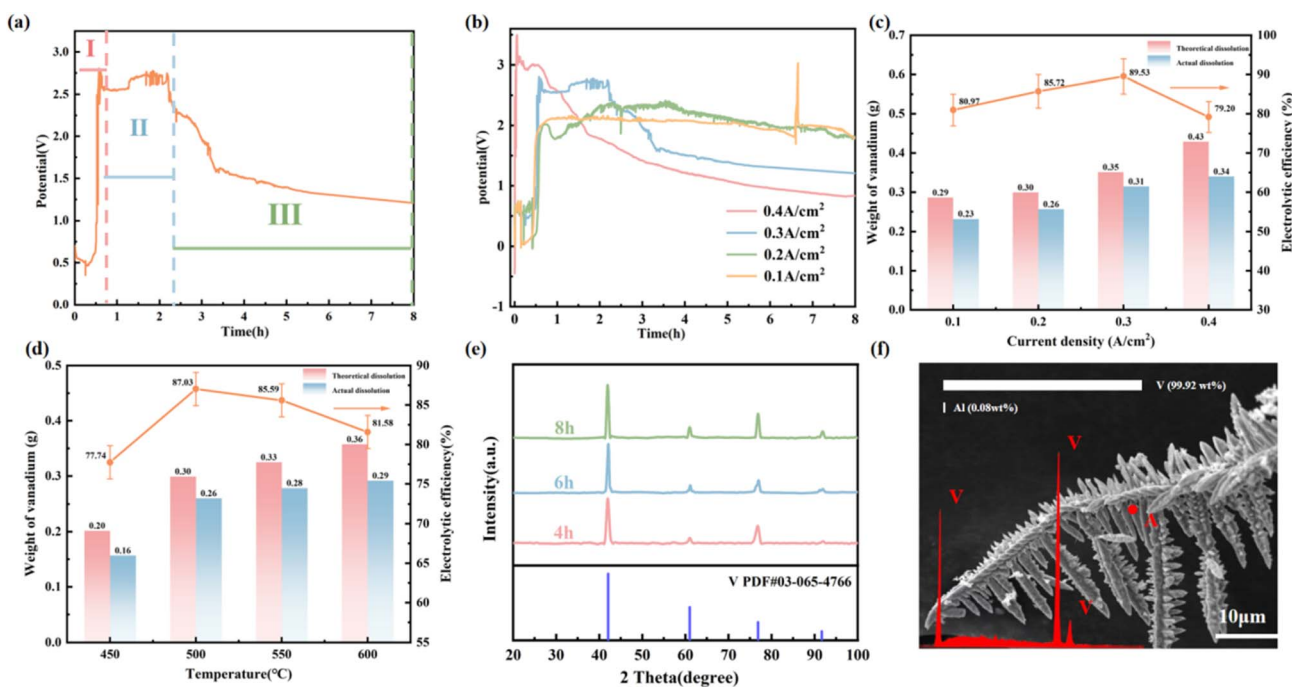

Fig. 4 (a) The evolution curves of voltages on electrolysis time at anode current density of 0.3 A cm^{-2} and cathode current density of 0.2 A cm^{-2}; (b) cell potential–time curves at various anode current densities (cathode current densities of 0.2 A cm^{-2}); (c) the electrolytic efficiency of different anode current densities, and the weight of vanadium about theoretical and actual dissolution; (d) effect of electrolysis temperature on electrolysis efficiency and vanadium weight; (e) XRD patterns of electrolysis products in different times; (f) SEM of metallic vanadium prepared from V–Al alloy.

presence of some moisture in the molten salt. In the second stage, as there is no molten salt, the voltage remains at a high level for a period of time. During this process, vanadium is almost not electro-deposited. This means that there is an induction period (IP) for the electro-deposition of vanadium.[34] In the third stage, the current rapidly decreases and then stabilizes, indicating that due to the electrochemical dissolution of V–Al, vanadium ions are introduced into the molten salt. The concentration of vanadium ions increases rapidly until it reaches saturation.

The anode current density determines the dissolution rate of the V–Al soluble anode. As shown in Fig. 4b, the influence of anode current densities ranging from 0.1 A cm^{-2} to 0.4 A cm^{-2} on metallic vanadium production was studied. A constant current electrolysis was performed at a fixed cathode current density of 0.2 A cm^{-2}. With the increase in anode current density, the IP time significantly decreased. This is due to the rapid electro-chemical dissolution of the V–Al soluble anode at higher anode current densities. As shown in Fig. 4c, when the anode current density increased from 0.1 A cm^{-2} to 0.4 A cm^{-2}, the mass of metallic vanadium also increased accordingly, from 0.23 g to 0.34 g. Meanwhile, the electrolytic efficiency firstly increased and then decreased, which may be due to the lower concentration of vanadium ions in the molten salt at lower anode current densities, thereby increasing the IP for vanadium electro-deposition and reducing the electrolytic efficiency. When the anode current density is too high, the concentration of vanadium ions

rapidly increases, and the ions cannot be completely deposited on the electrode, resulting in some vanadium loss. Therefore, the optimal anode current density is 0.3 A cm^{-2}.

Reaction temperature is also an important factor affecting electrolysis efficiency. As shown in Fig. 4d, the electrolytic efficiency increased from 77.74% at 450 °C to 87.03% at 500 °C. However, when the temperature increased further to 550 °C, the electrolytic efficiency significantly decreased to 85.59%. This is because, at higher temperatures, vanadium ions in the molten salt will volatilize along with chloride ions, thus reducing the actual concentration of vanadium ions and lowering the electrolytic efficiency. As shown in Fig. 4e, metallic vanadium can be obtained in a certain amount during the electrolysis process from 4 h to 8 h. This indicates that metallic vanadium can be deposited after 4 h.

Based on the above results, the optimal anode current density and electrolysis temperature are 0.3 A cm^{-2} and 500 °C, respectively. The electrolysis time is selected 6 h. The obtained product was analyzed by SEM and EDS (Fig. 4f), the metallic vanadium prepared using this method has a high purity. ICP detection was performed on it, and the impurity content of the product was found to be less than 0.11%.

3.2 Electrochemical behavior in molten salt

To investigate the electrochemical dissolution behavior of the soluble anode V–Al alloy, electrochemical tests were conducted
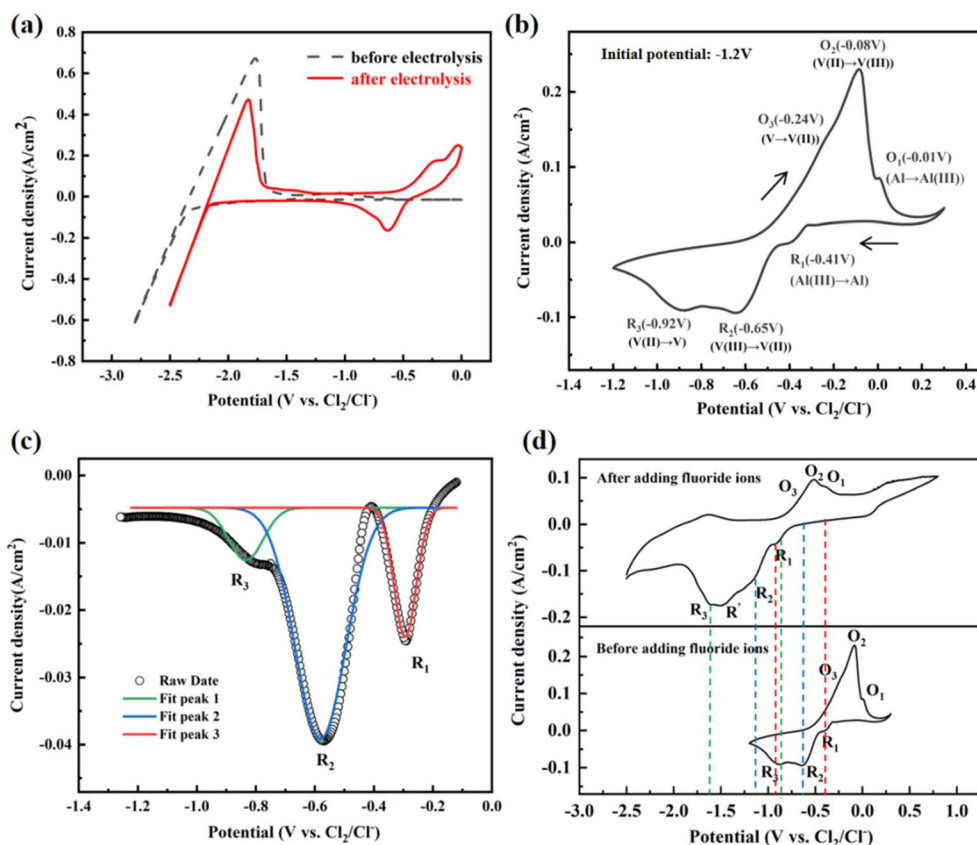

Fig. 5 (a) CV curves in KCl–LiCl molten salt before (black dashed line) and after (red line) V–Al alloy dissolution for 6 h; (b) CV curves in KCl–LiCl molten salt after V–Al alloy dissolution for 6 h; (c) SWV of vanadium ions dissolved from V–Al alloy; (d) comparison of CV curves before and after adding F ions.

in the KCl–LiCl molten salt. The cyclic voltammetry (CV) curve of the blank KCl–LiCl molten salt (Fig. 5a), as can be seen from the black dashed line, no obvious faradaic current was observed between −3V–0V, except for the redox peaks of the alkali metal element Li in the molten salt. This indicates that testing within this potential window does not affect the test results. To better identify the redox reactions, tests were conducted within an electrochemical window where no alkali metal deposition occurs. After electrolysis of the V–Al alloy at an anode current density of 0.3 A cm^{-2} and a cathode current density of 0.2 A cm^{-2} for 6 h, three pairs of oxidation-reduction peaks appeared (Fig. 5b), which preliminarily suggests that the reduction process involves three reduction steps. The reduction peaks R_1, R_2, and R_3 are located at −0.41 V, −0.65 V, and −0.92 V, respectively, while the corresponding oxidation peaks O_1, O_2, and O_3 are located at −0.01 V, −0.08 V, and −0.24 V.

To further verify the above conclusion, square wave voltammetry (SWV) was performed (Fig. 5c), with a scanning frequency of 30 Hz. Clearly, three reduction peaks, R_1, R_2, and R_3, can be observed, indicating that three reduction reactions occurred, and there is a good correspondence with the CV curve. The number of electrons transferred corresponding to the reduction peaks can be calculated using eqn (3):[35,36]

$$W_{\frac{1}{2}} = 3.52 \frac{RT}{nF} \qquad (3)$$

where $W_{\frac{1}{2}}$ is the half-wave width of the redox peak, R is the ideal gas constant (8.314 J mol^{-1} K^{-1}), and T is the absolute temperature (K).

The calculation of the SWV curve after Gaussian fitting yields $n_1 = 2.63 \approx 3$, $n_2 = 1.15 \approx 1$, and $n_3 = 1.71 \approx 2$. Therefore, R_1 transfers three electrons, R_2 transfers one electron, R_3 transfers two electrons. It can be preliminarily determined that R_1 is the process of Al(III) → Al, R_2 is the process of V(III) → V(II), R_3 is the process of V(II) → V.

The most commonly used electrolytes in electrolysis are chlorides and fluorides. Compared to Cl$^-$, F$^-$ exhibits stronger coordination capability. Adding F$^-$ to chlorides triggers ligand substitution, altering the coordination structure of vanadium ions in the molten salt. This modification consequently affects the electrochemical properties of metal ions in the molten salt and their reduction processes. To investigate the electrochemical behavior of the molten salt after the addition of F ions, 10 g of KF was added to 100 g of KCl–LiCl molten salt, and the electrolyte was subjected to electrolysis for 6 h at 500 °C. The CV curve obtained is shown in Fig. 5d. It can be observed that after the addition of F ions, the potential of R_1, R_2 and R_3 shifted leftward. The potential difference between R_1 and R_2 increased from 0.26 V to 0.4 V, which can better separate vanadium and aluminum. In addition, a new reduction peak R' was formed in the KCl–LiCl–KF molten salt, suggesting the formation of VCl$_i$F$_{6-i}^{3-}$,[37] while the bonding between Al and F was included in R_1, which was not obvious.

3.3 Analysis of bonding behavior between ions

In order to further investigate the bonding configuration of vanadium ions and aluminum ions, XPS analysis was performed on the electrolyte sample after electrolysis, as shown in Fig. 6a and b. It can be concluded that in molten salt, V mainly exists in the form of V^{3+} and V^{2+}, while Al mainly exists in the form of Al^{3+}. And it can be seen that after 1 h of electrolysis, there are no significant ions generation from Fig. 6c. Subsequently, ions begin to dissolve, and Raman shifts at 312 cm^{-1}, 439 cm^{-1}, 688 cm^{-1}, and 857 cm^{-1} mainly correspond to the formation of VCl$_6^{3-}$, VCl$_4^{2-}$. The Raman shift at 348 cm^{-1} mainly corresponds to the formation of AlCl$_4^-$. It can also be observed that after 6 h of electrolysis, most of the vanadium ions have been deposited, while a portion of the aluminum ions remain, which allows for a certain degree of separation between vanadium and aluminum.[33,38,39]

Meanwhile, we conducted MD simulations of the molten salt electrolysis process for vanadium production using the Forcete module of Materials Studio (MS). The study combines the Universal force field with the charge equilibration method, utilizing electrostatic charge calculations within a constant particle number volume temperature (NVT) ensemble. Employing the Andersen thermostat with a time step of 1.0 ps, the total simulation duration was set to 3000 ps. Molecular dynamics trajectories were sampled at 0 ps, 1000 ps, 2000 ps, and 3000 ps for subsequent analysis. As shown in the Fig. 6d, the structure of KCl–LiCl after 3000 ps of MD simulation can be observed that vanadium ions and aluminum ions form coordination structures with chloride (Cl) ions. The form of vanadium ions are VCl$_6^{3-}$, VCl$_4^{2-}$, VCl$_2$, VCl$_3$. The form of Al ions are AlCl$_4^-$. That is consistent with the results of the Raman analysis mentioned above. And Fig. 6e shows that the energy fluctuation in the simulated system is minimal, indicating that the system is in a state of equilibrium throughout the simulation process.

Density of States (DOS) analysis based on band theory helps further analyze the interactions in the molten salt. When the density of states of different orbitals near the valence band superimposes and peaks at the same energy, it is considered that there is interaction between ions, which is a clear sign of bonding, and this peak is called a hybridization peak.[40] Therefore, we added F ions to analyze the interactions between ions in the molten salt. As shown in Fig. 6f, the electronic orbitals near the lowest energy of −19 eV are occupied by F-2s orbitals, while the orbitals at an intermediate energy of −12 eV are occupied by Cl-2s orbitals. Near the Fermi level, the orbitals are mainly occupied by Cl-2p orbitals, with some hybridization with F-2p, V-3d, Al-3s, and Al-3p orbitals. This indicates that there are interactions between Cl, F, V, and Al in the molten salt.

The coordination tendencies of different metal cations with F$^-$ vary. To investigate the influence of F$^-$ on cation bonding in the KCl–LiCl system and reveal the structural evolution patterns and formation mechanisms of various ions in the KCl–LiCl–KF system, this study employed radial distribution function analysis to determine the probability of atomic occurrence within specific bonding regions, thereby identifying the bonding sequence of distinct ions. Furthermore, existing studies show that peaks below 3.5 Å are mainly formed by chemical bonds, while peaks above 3.5 Å are primarily formed by Coulomb and van der Waals interactions.[41] As shown in Fig. 6g, V^{3+} forms a strong peak at 2.37 Å, and Al^{3+} forms a strong peak at 2.28 Å,
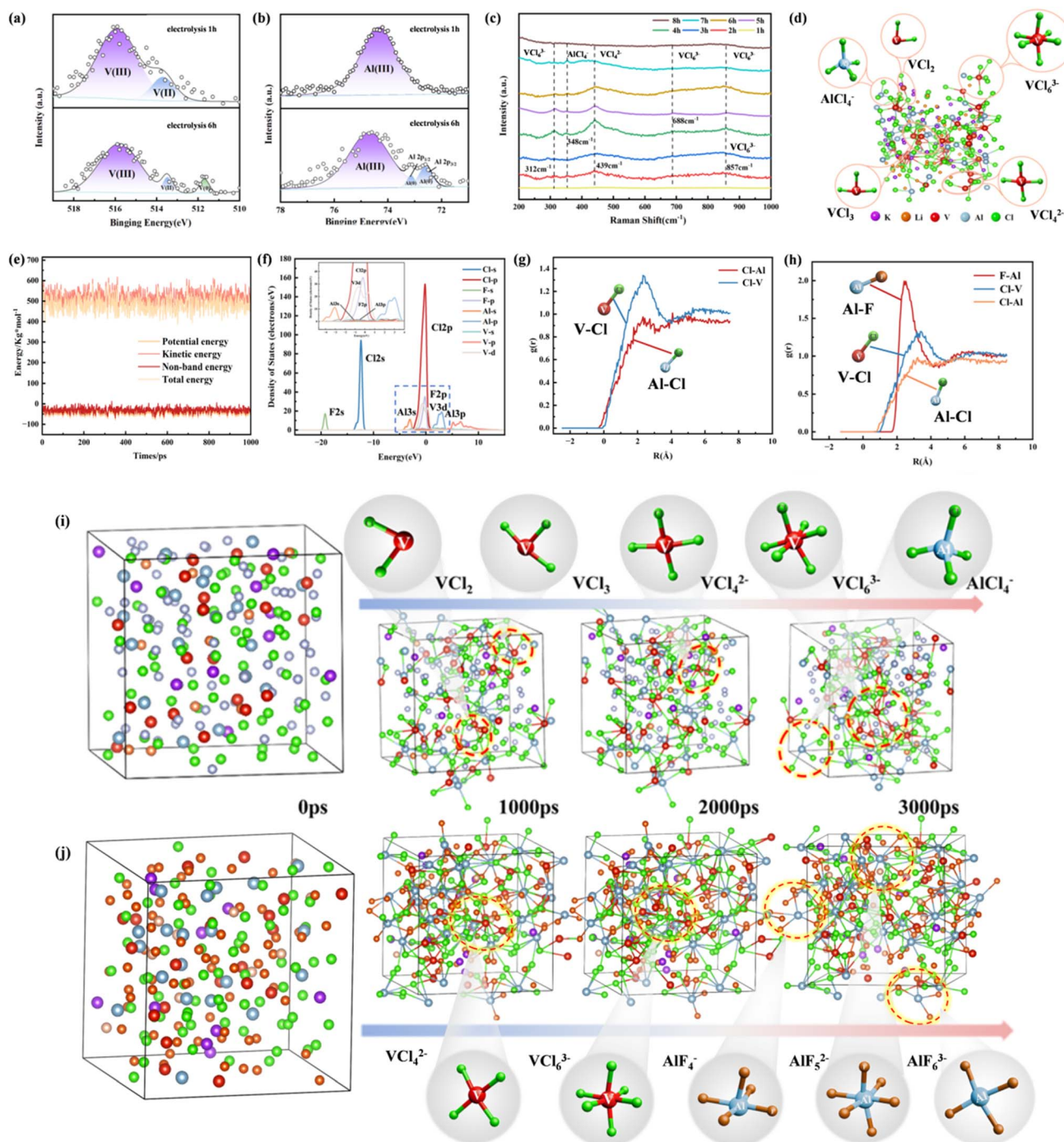
Fig. 6 XPS narrow spectrum corresponding to the bottom molten salt taken *in situ* at different times under constant anode current densities of 0.3 A cm^{-2}, cathode current densities of 0.2 A cm^2; (a) V; (b) Al; (c) raman spectra of molten salt dissolved from V−Al alloy in different times; (d) the final obtained structure after MD simulation (3000 ps); (e) MD simulation energy variation curve of molten salt system; (f) stable configuration density of states in molten salt system; the complex spatial configuration radial distribution function of V−Al in molten salt system (g) before adding F ions; (h) after adding F ions; a structural snapshot of vanadium ions in molten salt during 0−3000 ps (i) before adding F ions; (j) after adding F ions.

indicating that V and Al form chemical bonds with Cl, with the V−Cl bond having a stronger atomic interaction compared to the Al−Cl bond, making the V−Cl bond more likely to form. As shown in Fig. 6h, Al^{3+} forms a strong peak at 2.43 Å with F, and the atomic interaction strength is higher than that of V−Cl and Al−Cl, suggesting that Al forms a chemical bond with F first,

which facilitates the binding of more Cl ions to vanadium ions and promotes the dissolution of vanadium ions. Due to the high electronegativity of fluoride ions, their bond length with Al ions is shorter than that of V−Cl bonds, resulting in stable bond energy and Al ions are not easily deposited.
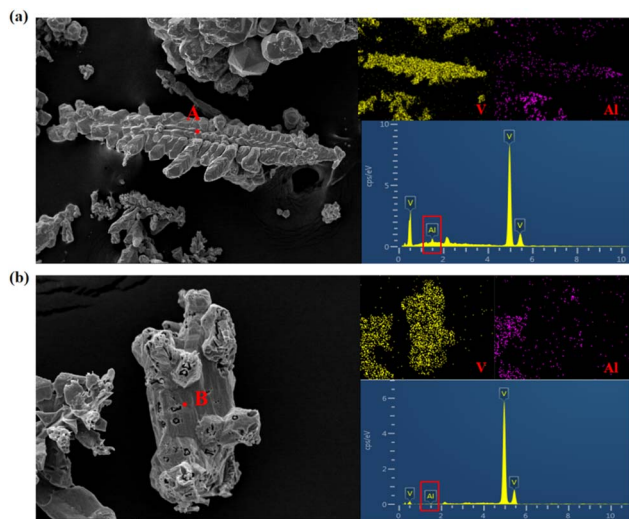
Fig. 7 SEM/EDS analysis results of cathode deposition products (a) before the addition of F⁻; (b) after the addition of F⁻.

Afterwards, exploring the dynamic dissociation of structures through the breaking and reorganization of chemical bonds, simulation methods can accurately track the movement of each atom, facilitating the study of the evolution of chemical bonds.[42] Fig. 6i presents snapshots of the molten salt structure at different time intervals. In the molten salt system, Li and K is randomly distributed in the simulation box, its small size and strong ionic nature prevent it from forming ion clusters with other ions. As time progresses, Cl ions in the molten salt gradually bond with vanadium ions, while aluminum ions directly bond with four Cl ions to form $AlCl_4^-$. In contrast, Fig. 6j shows that after the addition of F ions, aluminum ions preferentially bond with F ions, forming AlF_4^-, AlF_5^{2-}, and AlF_6^{3-} complexes. This process causes the Cl ions originally bonded to aluminum ions to coordinate with vanadium ions, thereby releasing more vanadium complexes, which aligns with the previously described results.

To further confirm the inhibitory effect of F⁻ on Al ions, we conducted SEM/EDS analysis on the deposition products obtained before and after the addition of F⁻. The results are as follows:

A comparison between Fig. 7a and b reveals that in the absence of F⁻, the surface morphology exhibits distinct features characteristic of aluminum distribution. In contrast, after the addition of F⁻, the correlation with aluminum is significantly reduced. Further EDS analysis indicates a notable decrease in the relative percentage of aluminum in the deposits, accompanied by an increase in the relative content of vanadium. This compositional change is highly consistent with the observed shift in SEM morphological correlations. These results directly demonstrate that the introduction of F⁻ effectively suppresses the aluminum deposition process.

3.4 Diffusion coefficient of vanadium ions in molten salt

To further investigate the mass transfer kinetics of vanadium ions in the KCl–LiCl molten salt, CV tests were performed at different scan rates within the same potential range. The curves

are shown in Fig. 8a, with an increase in scan rate, the peak current density gradually increases, and the peak potential shifts slightly negative. This suggests that the oxidation-reduction reaction is reversible. Next, the relationship between the maximum current density of the three reduction peaks and the square root of the scan rate was examined, as shown in Fig. 8b. After fitting the data, the peak current densities for all three reduction reactions exhibit a linear relationship with the square root of the scan rate, indicating that the reduction reactions at the electrode are diffusion-controlled in this experiment. The CV curve confirms that the redox peaks are reversible. Based on the characteristics of reversibility, it can be demonstrated that the corresponding oxidation process is also diffusion-controlled. The diffusion coefficient represents the rate at which ions diffuse in the molten salt and influences the electrolysis results and current efficiency. Therefore, the diffusion coefficient of V^{3+} in the molten salt was calculated.

There are two methods for calculating the diffusion coefficient; when both the reactant and the product are soluble, eqn (4) is used for the calculation:[43]

$$I_p = 0.4463 \frac{(nF)^{\frac{3}{2}} A D^{\frac{1}{2}} C \nu^{\frac{1}{2}}}{(RT)^{\frac{1}{2}}} \tag{4}$$

When the product is insoluble, eqn (5) can be used for the calculation:

$$I_p = 0.6103 \frac{(nF)^{\frac{3}{2}} A D^{\frac{1}{2}} C \nu^{\frac{1}{2}}}{(RT)^{\frac{1}{2}}} \tag{5}$$

where I_p is the peak current (A); A is the effective area of the working electrode (cm²); n is the number of electrons transferred in the reaction (mol); C is the concentration of the reactant (mol cm⁻³); F is the Faraday constant (C mol⁻¹); R is the ideal gas constant (8.314 J mol⁻¹ K⁻¹); T is the temperature (K); D is the diffusion coefficient (cm² s⁻¹); and ν is the scan rate (mV s⁻¹).

The diffusion coefficient of V^{3+} in the molten salt was calculated using eqn (4), and it was found to be 3.40×10^{-5} cm² s⁻¹.

Similarly, CV curves of molten salts after adding F ions were detected at different scan rates using the same method, as shown in Fig. 8c. The redox peak potential slightly shifted left with increasing scan rate, indicating that the corresponding reduction process is reversible. The relationship between the maximum current density of the reduction peaks and the square root of the scan rate was also investigated, as shown in Fig. 8d. After fitting the data, a linear relationship was observed, which indicates that the reduction reaction is still diffusion-controlled. The diffusion coefficient of V^{3+} in the molten salt was calculated using eqn (4), and the diffusion coefficient of V^{3+} in the molten KCl–LiCl–KF salt was found to be 4.08×10^{-5} cm² s⁻¹.

To further confirm the above findings, SWV tests were performed at different frequencies. The results are shown in Fig. 8e. As the scan frequency increases, the peak potential gradually shifts negatively, indicating that the oxidation-reduction reaction is reversible. Moreover, as shown in Fig. 8f, the peak current density exhibits a linear relationship with the
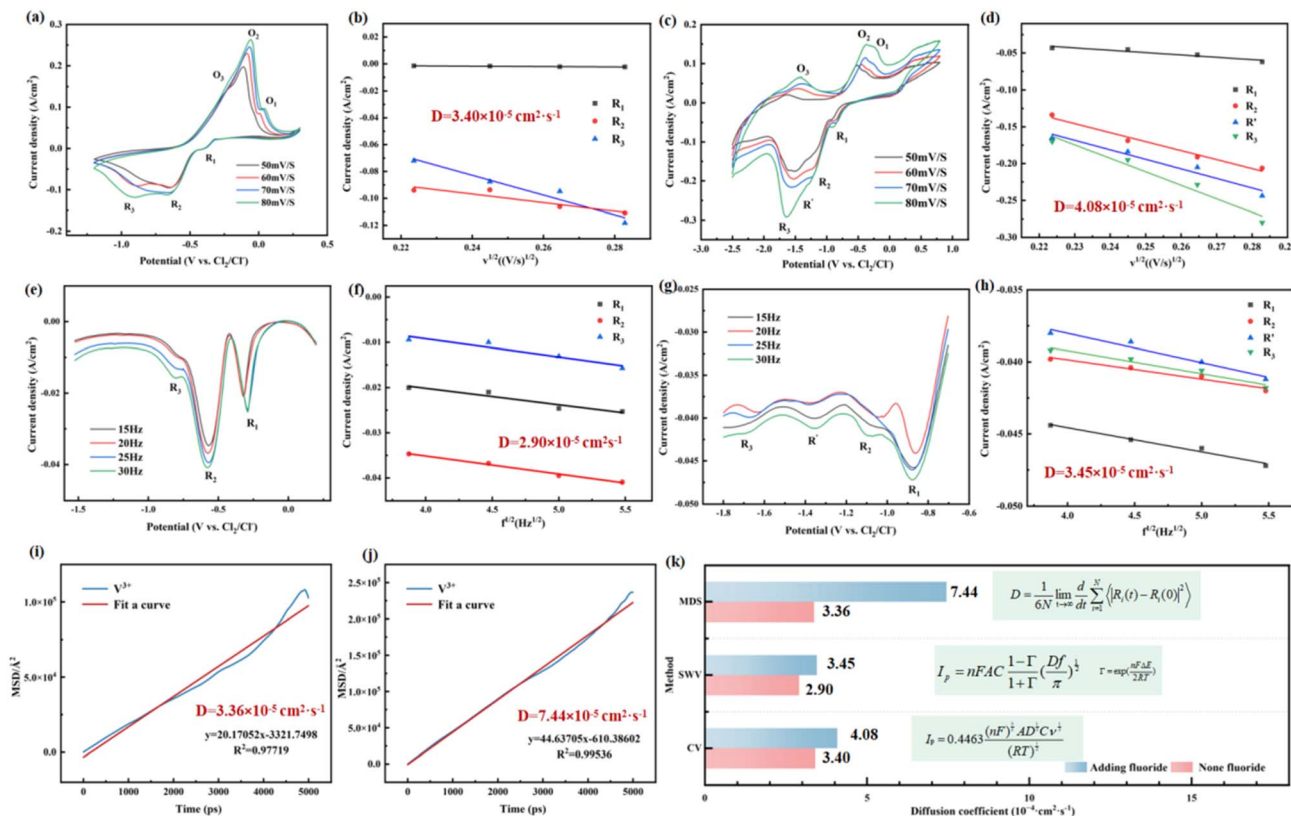
Fig. 8 (a) CV in KCl–LiCl after V–Al dissolution for 6 h at various scan rates; (b) the relationship between the current density and the square root of scan rate. Inset: relationship between peak potential and logarithm of scan rate; (c) CV in KCl–LiCl–KF after V–Al dissolution for 6 h at various scan rates. (d) The relationship between the current density and the square root of scan rate; (e) SWV in KCl–LiCl after V–Al dissolution for 6 h at various scan rates; (f) the relationship between the current density and the square root of frequency in KCl–LiCl; (g) SWV in KCl–LiCl–KF molten salt after V–Al dissolution for 6 h; (h) the relationship between the current density and the square root of frequency; MSD curve of V^{3+} (i) before adding F ions; (j) after adding F ions; (k) the diffusion coefficient calculated by three methods before and after adding F ions.

square root of the frequency. This is consistent with the results from CV. The diffusion coefficient of V^{3+} ions can also be calculated using eqn (6):[44]

$$I_p = nFAC\frac{1-\Gamma}{1+\Gamma}\left(\frac{Df}{\pi}\right)^{\frac{1}{2}}\Gamma = \exp\left(\frac{nF\Delta E}{2RT}\right) \quad (6)$$

where I_p is the peak current of the reaction (A); n is the number of electrons transferred in the reaction (mol); F is the Faraday constant (C mol^{-1}); C is the concentration of the reactant (mol cm^{-3}); A is the effective area of the working electrode (cm^2); R is the ideal gas constant (8.314 J mol^{-1} K^{-1}); T is the temperature (K); D is the diffusion coefficient (cm^2 s^{-1}); f is the frequency (Hz); and ΔE is the square wave amplitude (V).

The diffusion coefficient of V^{3+} in the molten KCl–LiCl molten salt was calculated to be 2.90×10^{-5} cm^2 s^{-1}.

Similarly, in the molten salt after adding F ions, SWV tests were performed at different scan frequencies, as shown in Fig. 8g. The number of reduction peaks is consistent with the CV curve, and the reduction peak R_1 is clearly visible. Moreover, as shown in Fig. 8h, the peak current density exhibits a linear relationship with the square root of the frequency. Thus, using eqn (6), the diffusion coefficient of V^{3+} ions in the molten KCl–LiCl–KF salt was calculated to be 3.45×10^{-5} cm^2 s^{-1}.

Furthermore, in MD simulations, the slope of the MSD curve, divided by 1/6, corresponds to the diffusion coefficient fitted according to Einstein diffusion equation, as shown in eqn (7):[45]

$$D = \frac{1}{6N}\lim_{t\to\infty}\frac{d}{dt}\sum_{i=1}^{N}\left\langle|R_i(t)-R_i(0)|^2\right\rangle \quad (7)$$

where N is the number of particles in the system, $\langle\rangle$ represents the average, $R_i(t)$ is the position vector at time t, and $R_i(0)$ is the initial position vector.

The MSD curve of the simulation system and the fitting curve are shown in Fig. 8i and j. The diffusion coefficient of unfluorinated V^{3+} is calculated to be 3.36×10^{-5} cm^2 s^{-1}, while the diffusion coefficient of fluorinated V^{3+} is 7.44×10^{-5} cm^2 s^{-1}, which is on the same order of magnitude as the electrochemical tests, and the diffusion rate increases after the introduction of F.

Based on the above data, we analyzed the diffusion coefficients of three methods in Fig. 8k. It can be concluded that after adding F ions, the diffusion rate of V^{3+} increased overall. This is due to the formation of a new reduction peak, which increases the concentration of vanadium ions and accelerates the mass transfer rate.

3.5 Nucleation mode of vanadium ions in molten salts

The nucleation of vanadium ions was studied using the instantaneous current method, and the time–current curve is shown in Fig. 9a and d. The voltage is set to the reduction voltage of R_2 and R_3, which are -0.6 V and -0.9 V. Initially, the current increased over time, then rapidly decreased, and finally stabilized.

Generally, there are two different types of nucleation: instantaneous nucleation and continuous nucleation. The nucleation process model is as follows:[46,47]

For instantaneous nucleation:

$$\left(\frac{I}{I_m}\right)^2 = 1.9542 \frac{\left[1 - \exp\left(-1.2564\left(\frac{t}{t_m}\right)\right)\right]^2}{\left(\frac{t}{t_m}\right)} \quad (8)$$

For continuous nucleation:

$$\left(\frac{I}{I_m}\right)^2 = 1.2254 \frac{\left[1 - \exp\left(-2.3367\left(\frac{t}{t_m}\right)^2\right)\right]^2}{\left(\frac{t}{t_m}\right)} \quad (9)$$

where I_m is the peak current, t_m is the peak time.

Calculating the theoretical model and experimental values in the dimensionless plots of $(I/I_m)^2$ and (t/t_m) using eqn (8) and (9). It can be concluded that the nucleation of vanadium ions involves both instantaneous nucleation and continuous nucleation by fitting and analyzing the data (Fig. 9b and e). The obtained metal vanadium product was washed with deionized water, soaked in dilute hydrochloric acid to remove aluminum and other impurities, and then vacuum-dried and collected. The product was characterized by scanning electron microscopy (SEM), as shown in Fig. 9c and f. The product exhibited two morphologies: dendritic and foamy, where the dendritic morphology was formed by continuous nucleation and the foamy morphology by instantaneous nucleation.

The formation of the aforementioned morphologies is primarily related to the current density and vanadium ion concentration during the electrolysis process. In the initial stages of electrolysis, the high ion concentration prevents ion depletion near the cathode. At this point, the rate of crystal growth outpaces the rate of nucleation during deposition, favoring rapid nucleation and the development of simpler morphologies, thereby resulting in a foamy structure. As electrolysis progresses and ion concentrations decrease,
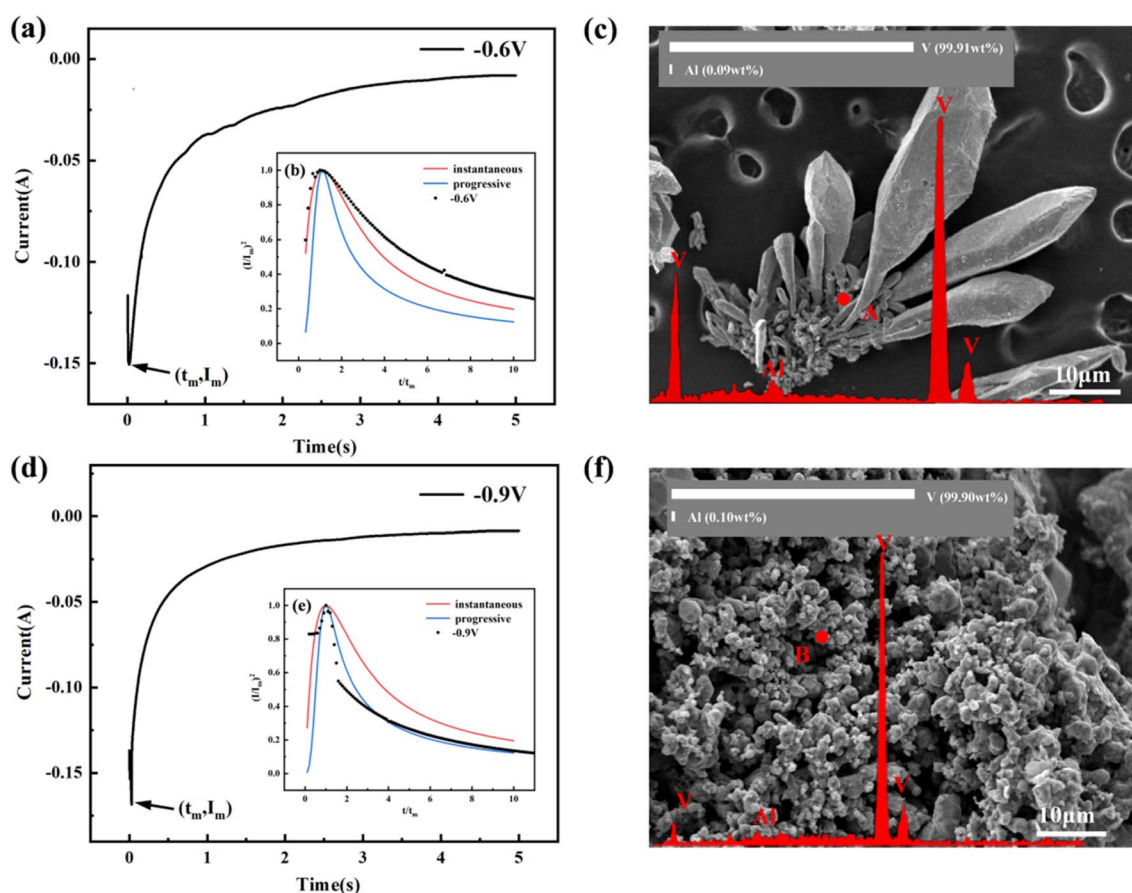

Fig. 9 (a) Current curves in LiCl–KCl molten salt at −0.6 V; (b) plot of $(I/I_m)^2$ and (t/t_m) compared with theoretical curves at −0.6 V; (c) SEM images of the transient nucleation in the molten salt and the results of EDS analysis at point A; (d) current curves in LiCl–KCl molten salt at −0.9 V; (e) plot of $(I/I_m)^2$ and (t/t_m) compared with theoretical curves at −0.9 V; (f) SEM images of the progressive nucleation in the molten salt and the results of EDS analysis at point B.

concentration polarization occurs near the cathode. Under these conditions, the nucleation of vanadium ion deposition becomes more challenging, and crystal growth is hindered, leading to the formation of dendritic structures.

Finally, the mechanism of the whole electrolysis process is analyzed in Fig. 10. During the anodic dissolution process, an external voltage is applied to the anode by a DC power source, causing the V–Al alloy to undergo an oxidation reaction under electrochemical influence. Vanadium and aluminum lose electrons and enter the electrolyte, transforming into V^{2+}, V^{3+}, and Al^{3+}. The oxidation process of vanadium is influenced by the electrolyte composition and current density. At lower current densities, the voltage is reduced, and the oxidation is predominantly dominated by V^{3+} ions. The dissolution process is as follows:
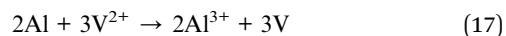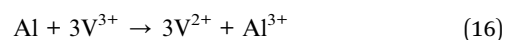
$$V \rightarrow V^{2+} + 2e^- \tag{10}$$

$$V \rightarrow V^{3+} + 3e^- \tag{11}$$

$$Al \rightarrow Al^{3+} + 3e^- \tag{12}$$

Then in the KCl–LiCl–KF molten salt system, the V^{2+}, V^{3+}, and Al^{3+} ions released during anode dissolution enter the molten salt and undergo coordination reactions with Cl^- and F^- ions. At elevated temperatures, the ions within the molten salt continuously reorganize, and their coordination structures dynamically transform in response to temperature, ion concentration, and electric field variations. Initially, V^{2+} bonds with Cl^- to form VCl_2, while V^{3+} bonds with Cl^- to form VCl_3. These compounds further interact with excess Cl^- in the KCl–LiCl–KF system to form more stable chloro-complex ions, such as VCl_4^{2-} and VCl_6^{3-}. In the presence of F^-, partial substitution of Cl^- by F^- occurs in the V–Cl coordination structures, generating mixed chloro–fluoro complexes like $VCl_iF_{6-i}^{3-}$. Similarly, Al^{3+} participates in analogous coordination reactions. Owing to the higher bond strength of Al–F compared to Al–Cl, Al^{3+} readily combines with F^- in the KCl–LiCl–KF system to

form potential complexes such as AlF^{4-}, AlF_5^{2-}, and AlF_6^{3-}. Concurrently, in chloride-dominated molten salts, Al^{3+} may also form chloro-complexes like $AlCl_4^-$. However, these chloro-complexes exhibit lower stability and are prone to substitution by F^- due to the stronger affinity of Al^{3+} for fluoride ligands.

Ultimately, the complexes in the molten salt gradually migrate toward the cathode under the influence of the electric current. The addition of an appropriate amount of F^- accelerates ion mass transfer rates, thereby promoting the deposition of metal at the cathode. On the cathode surface, vanadium ions in the molten salt are reduced to metallic vanadium. The main reaction equation of vanadium complexes during cathodic deposition is as follows:

$$VCl_6^{3-} + e^- \rightarrow VCl_4^{2-} + 2Cl^- \tag{13}$$

$$VCl_4^{2-} + 2e^- \rightarrow V + Cl^- \tag{14}$$
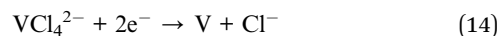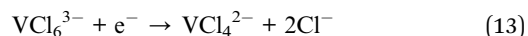
While aluminum ions largely coordinated with F^- remain in ionic form under specific potential conditions, enabling the purified deposition of metallic vanadium. A small amount of deposited metallic aluminum undergoes thermal reduction reactions with undeposited vanadium ions at high temperatures, where V^{2+} or V^{3+} are reduced to V or V^{2+}, and Al is oxidized back to Al^{3+}, re-entering the electrolyte to continue participating in the reaction cycle. The main reaction equation is as follows:

$$Al^{3+} + 3e^- \rightarrow Al \tag{15}$$

$$Al + 3V^{3+} \rightarrow 3V^{2+} + Al^{3+} \tag{16}$$

$$2Al + 3V^{2+} \rightarrow 2Al^{3+} + 3V \tag{17}$$

4. Conclusion

This work validates a novel method for producing metallic vanadium through molten salt electrolysis using a soluble V–Al alloy anode. Compared to the conventional process of aluminothermic reduction-vacuum electron beam melting for vanadium production, the new technique employs lower-purity vanadium–aluminum alloy as feedstock. It replaces the dual electron beam melting steps with single-step electrolytic refining, achieving higher-purity metallic vanadium. The research systematically investigates the effects of key electrolytic parameters including anode current density, reaction temperature, and duration to determine optimal operating conditions. The electrochemical behavior and bonding behavior between ions in molten salt was studied. The results show that there are three redox reactions in molten salt, R_1 corresponds to Al(III) → Al, R_2 corresponds to V(III) → V(II), and R_3 corresponds to V(II) → V. The forms of V ions are VCl_6^{3-}, VCl_4^{2-}, VCl_2, VCl_3. The form of Al ions are $AlCl_4^-$. After adding F ions, the potential of V^{3+}, V^{2+} and Al^{3+} shifted leftward. The potential difference between V^{3+} and Al^{3+} increased from 0.26 V to 0.4 V. And Al forms a chemical bond with F first, which facilitates the binding of more Cl ions to vanadium ions and promotes the dissolution of vanadium ions.
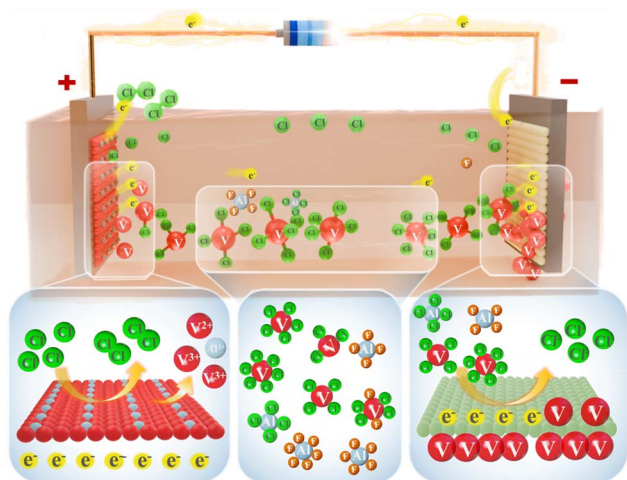

Fig. 10 Mechanism diagram of metallic vanadium preparation by molten salt electrolysis.

Subsequently, the diffusion coefficient and nucleation mode of V^{3+} were analyzed. All of the reversible processes are controlled by diffusion. The diffusion coefficient of V^{3+} was calculated by CV, SWV and MDS. Before adding F ions, the calculated diffusion coefficients were 3.40×10^{-5} cm^2 s^{-1}, 2.90×10^{-5} cm^2 s^{-1} and 4.12×10^{-5} cm^2 s^{-1}. After adding F ions, the calculated diffusion coefficients were 4.08×10^{-5} cm^2 s^{-1}, 3.36×10^{-5} cm^2 s^{-1} and 7.44×10^{-5} cm^2 s^{-1}. It can be concluded that with the addition of F ions, the diffusion rate of V^{3+} accelerates. And it is determined that vanadium ions undergo both instantaneous nucleation and continuous nucleation on the tungsten electrode surface. This work provides a new and feasible method for the production of metallic vanadium.

Author contributions

Qiwen Zhang: conceptualization, investigation, methodology, writing-original draft, writing-review & editing. Yong Fan: writing-review & editing, supervision. Yimin Zhang: writing-review & editing, supervision. Peng Liu: data computation. Hong Liu: writing-review & editing, supervision. Zihanyu Zhang: data computation. Xiuqiong Fu: data computation.

Conflicts of interest

The authors declare that they have no known competing financial interests or personal relationships that could have appeared to influence the work reported in this paper.

Data availability

All data included in this study are available upon request by contact with the corresponding author.

Acknowledgements

References

1 Y. Guo, H.-Y. Li, S. Shen, C. Wang, J. Diao and B. Xie, *Hydrometallurgy*, 2020, **198**, 105509.

2 A. Biswas, C. Sahoo, W.-T. Du, I.-H. Jung and M. Paliwal, *Metall. Mater. Trans. B*, 2021, **52**, 956–967.

3 C. Choi, S. Kim, R. Kim, Y. Choi, S. Kim, H. Jung, J. H. Yang and H.-T. Kim, *Renewable Sustainable Energy Rev.*, 2017, **69**, 263–274.

4 P. Zhou, Z. Cao, X. Xiao, Z. Jiang, L. Zhan, Z. Li, L. Jiang and L. Chen, *Int. J. Hydrogen Energy*, 2022, **47**, 1710–1722.

5 Z.-M. Cao, P.-P. Zhou, X.-Z. Xiao, L.-J. Zhan, Z.-F. Jiang, S.-M. Wang, L.-J. Jiang and L.-X. Chen, *Rare Met.*, 2022, **41**, 2588–2594.

6 H. Arabi, M. Ketabchi and S. H. N. Alhosseini, *Rare Met.*, 2022, **41**, 2732–2738.

7 G. Zhang, T. Zhang, G. Lü, Y. Zhang, Y. Liu and Z. Liu, *Int. J. Miner., Metall. Mater.*, 2015, **22**, 21–26.

8 S. Wang, S. Li, L. Wan and C. Wang, *Int. J. Miner., Metall. Mater.*, 2012, **19**, 212–216.

9 S. Liu, Y. Zhen, X. He, L. Wang and K. Chou, *Int. J. Miner., Metall. Mater.*, 2020, **27**, 1678–1686.

10 F. Gao, A. U. Olayiwola, B. Liu, S. Wang, H. Du, J. Li, X. Wang, D. Chen and Y. Zhang, *Miner. Process. Extr. Metall. Rev.*, 2022, **43**, 466–488.

11 K. Wang, Q. Wang, J. He and C. Liu, *Steel Res. Int.*, 2008, **79**, 712–716.

12 P. K. Tripathy and A. K. Suri, *High Temp. Mater. Processes*, 2002, **21**, 127–138.

13 A. Miyauchi and T. H. Okabe, *Mater. Trans.*, 2010, **51**, 1102–1108.

14 P. Tripathy, *Mater. Res. Bull.*, 2003, **38**, 1175–1182.

15 P. K. Tripathy and J. M. Juneja, *High Temp. Mater. Processes*, 2004, **23**, 237–246.

16 S. Li, Y. Che, J. Song, Y. Shu, J. He, B. Xu and B. Yang, *Sep. Purif. Technol.*, 2021, **274**, 118803.

17 T. Yin, Y. Xue, Y. Yan, Z. Ma, F. Ma, M. Zhang, G. Wang and M. Qiu, *Int. J. Miner., Metall. Mater.*, 2021, **28**, 899–914.

18 Y. Liu, M. Tang, S. Zhang, Y. Lin, Y. Wang, Y. Wang, Y. Dai, X. Cao, Z. Zhang and Y. Liu, *Int. J. Miner., Metall. Mater.*, 2022, **29**, 479–489.

19 Y. Kong, B. Li, J. Chen, K. Liu and Q. Han, *Electrochim. Acta*, 2020, **342**, 136081.

20 W. Weng, M. Wang, X. Gong, Z. Wang, D. Wang and Z. Guo, *Int. J. Refract. Met. Hard Mater.*, 2016, **55**, 47–53.

21 E. Ahmadi, R. O. Suzuki, T. Kikuchi, T. Kaneko and Y. Yashima, *Int. J. Miner., Metall. Mater.*, 2020, **27**, 1635–1643.

22 G. Z. Chen, D. J. Fray and T. W. Farthing, *Metall. Mater. Trans. B*, 2001, **32**, 1041–1052.

23 G. Z. Chen, *Int. J. Miner., Metall. Mater.*, 2020, **27**, 1572–1587.

24 R. O. Suzuki and H. Ishikawa, *Miner. Process. Extr. Metall.*, 2008, **117**, 108–112.

25 D. E. Woolley, U. B. Pal and G. B. Kenney, *High Temp. Mater. Processes*, 2001, **20**, 209–218.

26 J.-L. An, M.-Y. Wang, Y.-Z. Jia, J.-T. Zhang, B.-Y. Feng and S.-Q. Jiao, *Rare Met.*, 2024, **43**, 3961–3973.

27 Z. Liu, M. Sheng, Y. He, H. Zhou, J. Huang, X. Luo and Y. Zhang, *J. Mol. Liq.*, 2022, **347**, 117992.

28 D. Wang, S. Pang, C. Zhou, Y. Peng, Z. Wang and X. Gong, *Int. J. Miner., Metall. Mater.*, 2020, **27**, 1618–1625.

29 J. Song, J. Xiao and H. Zhu, *J. Electrochem. Soc.*, 2017, **164**, E321–E325.

30 S. Liu, S. Li, C. Liu, J. He and J. Song, *Int. J. Miner., Metall. Mater.*, 2023, **30**, 868–876.

31 I. B. Polovov, M. V. Chernyshov, V. A. Volkovich, G. A. Nechkin, O. I. Rebrin, A. N. Rylov and T. R. Griffiths, *ECS Trans.*, 2009, **16**, 479–487.

32 S. Li, Y. Che, C. Li, Y. Shu, J. He, B. Yang and J. Song, *J. Magnesium Alloys*, 2022, **10**, 721–729.

33 R. Yuan, C. Lv, H. Wan, S. Li, Y. Che, Y. Shu, J. He and J. Song, *J. Electroanal. Chem.*, 2021, **891**, 115259.

34 J. An, M. Wang, Y. Jia, Y. Chen and S. Jiao, *Sep. Purif. Technol.*, 2022, **295**, 121361.

35 J. J. O'Dea, J. Osteryoung and R. A. Osteryoung, *Anal. Chem.*, 1981, **53**, 695–701.

36 K. Aoki, K. Tokuda, H. Matsuda and J. Osteryoung, *J. Electroanal. Chem. Interfacial Electrochem.*, 1986, **207**, 25–39.

37 R. Yuan, C. Lü, H. Wan, S. Li, Y. Che, J. He and J. Song, *Trans. Nonferrous Met. Soc. China*, 2022, **32**, 2736–2745.

38 C. C. Alves, T. B. C. Campos and W. A. Alves, *Spectrochim. Acta, Part A*, 2012, **97**, 1085–1088.

39 L. Legrand, A. Tranchant, R. Messina, F. Romain and A. Lautie, *Inorg. Chem.*, 1996, **35**, 1310–1312.

40 M. Todorova, K. Reuter and M. Scheffler, *J. Phys. Chem. B*, 2004, **108**, 14477–14483.

41 J. Zeng, J. Zhang and X. Gong, *Comput. Theor. Chem.*, 2011, **963**, 110–114.

42 S. Dutta, S. De, S. Bose, E. Mahal and D. Koley, *Eur. J. Inorg. Chem.*, 2020, **2020**, 638–655.

43 S. Liu, L. Wang, K. Chou and R. V. Kumar, *J. Alloys Compd.*, 2019, **803**, 875–881.

44 Y. Song, S. Jiao, L. Hu and Z. Guo, *Metall. Mater. Trans. B*, 2016, **47**, 804–810.

45 S.-Q. Hu, A.-L. Guo, Y.-G. Yan, X.-L. Jia, Y.-F. Geng and W.-Y. Guo, *Comput. Theor. Chem.*, 2011, **964**, 176–181.

46 M. R. Khelladi, L. Mentar, A. Azizi, A. Sahari and A. Kahoul, *Mater. Chem. Phys.*, 2009, **115**, 385–390.

47 M. M. Tylka, J. L. Willit and M. A. Williamson, *J. Electrochem. Soc.*, 2017, **164**, H5327–H5335.